ACS APPLIED MATERIALS & INTERFACES

www.acsami.org

Research Article

Flexible Metal Electrodes by Femtosecond Laser-Activated Deposition for Human−Machine Interfaces

Yaqiang Ji, Yuxuan Liao, Haihui Li, Yuhang Cai, Dongliang Fan, Qian Liu, Shubin Huang, Renjie Zhu, Shuai Wang, Hongqiang Wang,* and Liang Guo*

Cite This: *ACS Appl. Mater. Interfaces* 2022, 14, 11971−11980

Read Online

ACCESS | Metrics & More | Article Recommendations | Supporting Information

ABSTRACT: Flexible metal electrodes are essential for flexible electronics, where the main challenge is to obtain mask-free patterned metals directly on substrates such as poly(dimethylsiloxane) (PDMS) at low cost. This work highlights a feasible strategy named femtosecond laser-activated metal deposition for electroless deposition of metals (Cu, Ni, Ag, and Au) on PDMS, which is suitable for maskless and low-cost fabrication of metal layers on PDMS and even on other materials of different natures including polyethylene terephthalate, paper, Si, and glass. The electrical conductivity of the PDMS/Cu electrode is comparable to that of bulk Cu. Moreover, robust bonding at the PDMS/Cu interface is evidenced by a scotch tape test and bending test of more than 20,000 cycles. Compared with previous studies using a nanosecond laser, the restriction on absorbing sensitizers could be alleviated, and catalysts could originate from precursors without polymer substrates under a femtosecond laser, which may be attributed to nonlinear absorption and ultrashort heating time with the femtosecond laser. Implementing a human−machine interface task is demonstrated by recognizing hand gestures via a multichannel electrode array with high fidelity to control a robot hand.

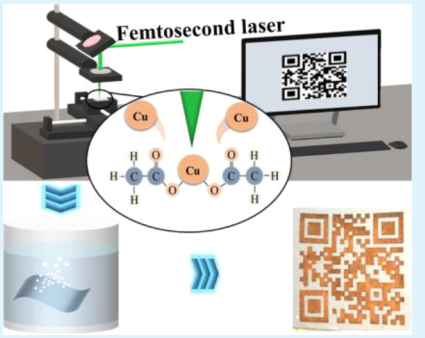

KEYWORDS: *flexible electrodes, femtosecond laser, poly(dimethylsiloxane), metal deposition, strong adhesion*

1. INTRODUCTION

There is an ever-increasing need to research flexible electronics because of their great potential applications in human−machine interfaces,[1,2] wearable displays,[3,4] soft robotics,[5,6] electronic skins,[7,8] and so forth. As the primary transporting channel for electrical signals, flexible electrodes with good electrical and mechanical properties are always desired for better performance of the devices.[9] Novel conductive materials, such as liquid metals,[10,11] carbon materials,[12,13] and conducting polymers,[14,15] have been implemented in flexible electronics, but they are not as good as conventional metals due to the electrical conductivity and cost.[16,17] Metal foils usually suffer from high rigidity. Therefore, thin metal layers physically or chemically deposited on flexible substrates are preferred for flexible electronics.[18,19]

Many methods have been investigated on depositing metal films on flexible substrates, including physical vapor deposition (PVD),[20] applying liquid metals,[10,11] electroless deposition (ELD),[21] etc. PVD typically requires vacuum and subsequent patterning with photolithography, which is often costly and time-consuming.[20] Liquid metals have attracted much attention due to excellent properties such as nontoxicity, high electrical/thermal conductivity, deformability, self-healing ability, and surface functionalization accessibility,[22,23] but the limited wettability from the high surface tension is unfavorable in many flexible applications.[24] In general, ELD is a promising choice for the metallization of flexible substrates with both high electrical conductivity and low cost, which usually relies on an autocatalytic redox reaction to deposit a thin metal film on a catalyst-preloaded substrate.

There are many choices for flexible substrates, including paper,[25] cotton,[26] polyethylene terephthalate (PET),[27] polyimide,[28] poly(vinylidene fluoride),[29] poly(dimethylsiloxane) (PDMS),[30] etc. PDMS is one of the best materials because of simple and inexpensive fabrication, mechanical flexibility and stability, high dielectric constant, optical transparency, biocompatibility, and biostability.[31,32] However, it is difficult to integrate metals on the PDMS surface without a special treatment due to its low surface energy.[33] To date, limited success is achieved with sensibilization and chemical activation before deposition. To the best of our knowledge, one of the most popular techniques for depositing metal films on PDMS depends on surface-grafted polymers,[34−37] which has been successfully applied to deposit different metals on a wide variety of substrates. The key of this technique is to efficiently adsorb catalyst ions for ELD on flexible substrates modified by

Received: January 8, 2022
Accepted: February 15, 2022
Published: February 25, 2022

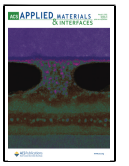

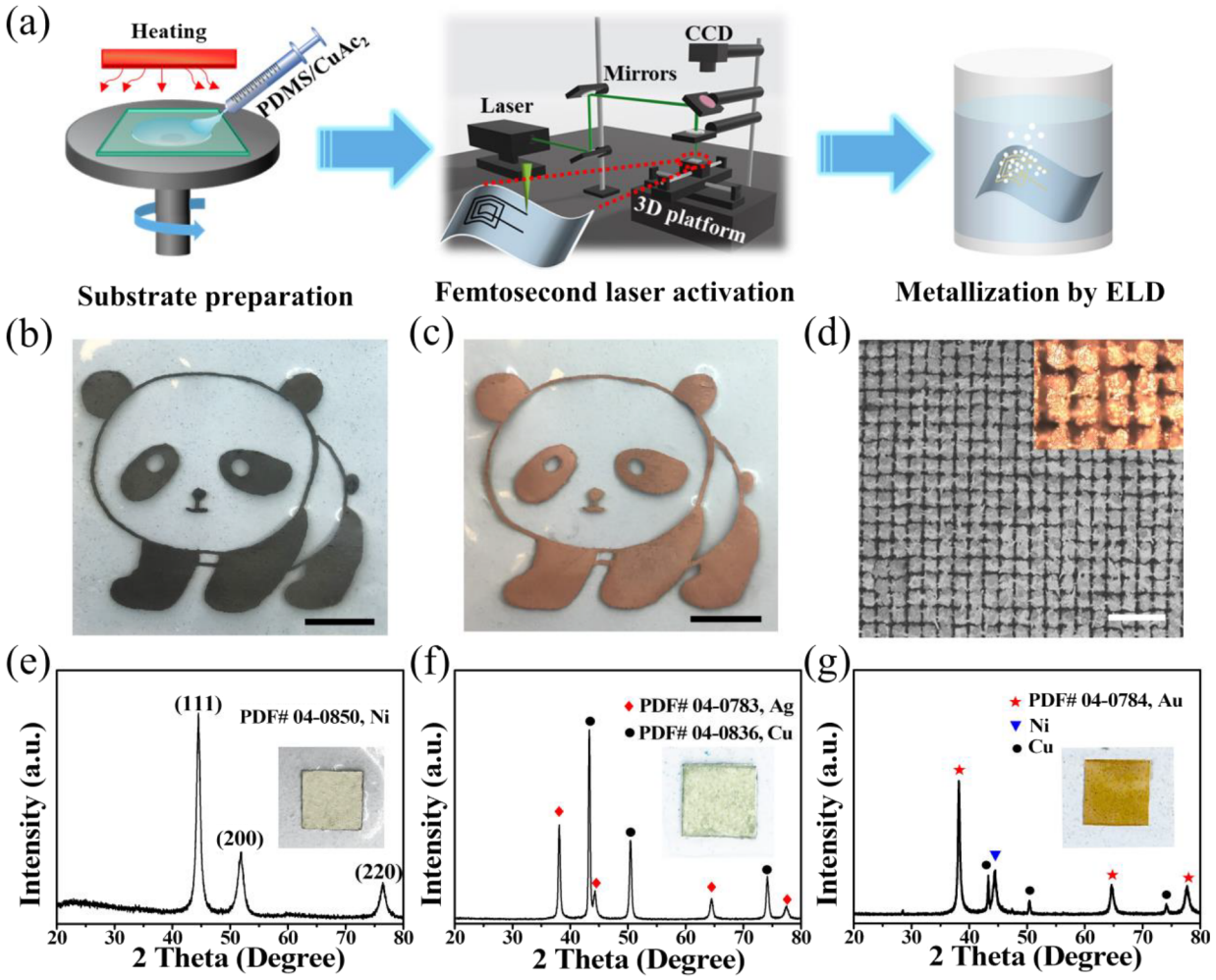

Figure 1. (a) Schematic of the fabrication process of FLAMD. (b,c) Photographs showing a panda on the PDMS/$CuAc_2$ film after femtosecond laser activation and after ELD (scale bars: 10 mm). (d) SEM image of the obtained Cu coating by a cross-scan approach with an interval of 50 μm (scale bar: 200 μm). The inset shows the optical image. (e–g) XRD spectra and optical images of the obtained metals (Ni, Ag, and Au) on PDMS.

interfacial polymer layers with functional groups. Although the technique has been developed through the decades, it requires difficult surface pretreatments and demanding synthesis protocols.[38,39]

Laser direct writing is a manufacturing technology that uses a computer-controlled laser or sample scanner to create complex structures directly on various materials in a maskless manner.[40−42] Recently, using this technology, a Cu depositing method has attracted increasing attention[43−45] in which a Cu layer is coated on a polymer substrate by an infrared nanosecond laser irradiation first (Cu particles are generated from polymers doped with specific sensitizers to work as the catalyst in the next step) and then ELD.[43] However, the previous work tried only a few types of sensitizers in the presence of polymers, pointing out the restriction of laser-absorbing sensitizers and the necessity of polymers as carbon sources for reducing environments.[44] Femtosecond laser processing may solve the above problems because it can induce nonlinear absorption, releasing the selection of absorbers, and has ultrashort heating time, which weakens oxidation in the air even without reductants.

Herein, we propose a feasible strategy, combining low-cost ELD and femtosecond laser processing, called femtosecond laser-activated metal deposition (FLAMD), which allows ambient deposition of metal films on PDMS with high electrical conductivity, strong adhesion, and high reliability. FLAMD could simplify the fabrication of metal patterns on PDMS compared with the current techniques such as PVD and surface-grafted polymerization. Moreover, we demonstrate that FLAMD is effective for depositing different kinds of metals (Cu, Ni, Ag, and Au) on materials besides PDMS and of different natures, including PET, paper, Si, and glass. Compared with the infrared nanosecond laser, the femtosecond laser possesses less limitation on absorbing sensitizers, and polymer substrates are no longer necessary for catalyst generation from precursors. With FLAMD, a multichannel electrode array with high fidelity has been fabricated and applied for hand gesture recognition and control of a robot hand to demonstrate a human−machine interaction application.

2. FABRICATION ROUTE

Figure 1a presents the primary process of FLAMD, including flexible substrate preparation, femtosecond laser activation, and metallization by ELD. Taking Cu deposition as an example, 1 wt % $CuAc_2$ was added into the PDMS matrix to fabricate a ∼100 μm thick flexible substrate. As shown in Supplementary Note 1, the transmittance of PDMS/$CuAc_2$ is above 87% between 400 and 1000 nm, and the film could stand on a dandelion flower without obvious deformation of the stem, showcasing the

https://doi.org/10.1021/acsami.2c00419
ACS Appl. Mater. Interfaces 2022, 14, 11971−11980

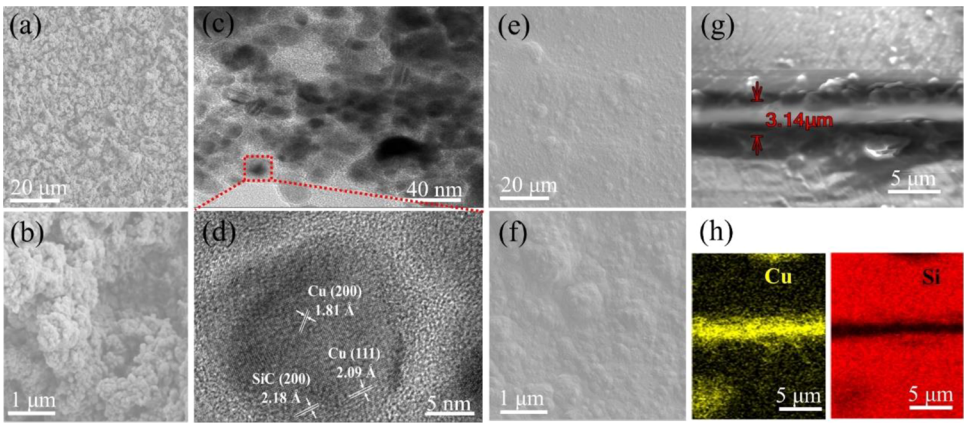

Figure 2. (a,b) SEM images of the sample after femtosecond laser activation. (c,d) TEM image of the sample after femtosecond laser activation. (e,f) SEM images of the sample after ELD for 60 min. (g,h) SEM and EDX mapping images of the obtained Cu wire.

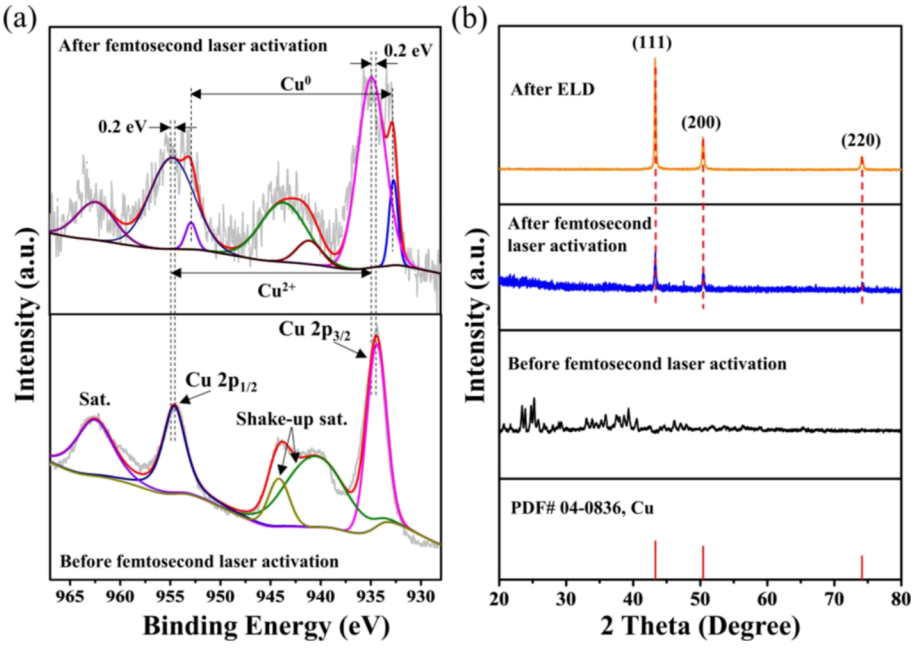

Figure 3. (a) High-resolution XPS Cu 2p spectra of the sample before and after femtosecond laser activation. The gray and red lines represent the raw data and the fitting curve, respectively. (b) XRD spectra of the sample before, after femtosecond laser activation, and after ELD.

ultralightweight nature. Then, the desired pattern was created on the substrate by femtosecond laser activation at 515 nm, through which catalytic sites for ELD were generated on the irradiated area. The results of ELD could be controlled by adjusting the scanning speed of the sample stage and the repetition rate of the femtosecond laser. According to the parameter test (Supplementary Note 2), we set the fluence, the scanning speed, and the repetition rate as 22 mJ cm^{-2}, 10 mm s^{-1}, and 50 kHz, respectively. Finally, during the ELD process, the copper ions (Cu^{2+}) in the solution were gradually reduced by formaldehyde in the presence of catalytic sites. After deposition of a small amount of Cu, the redox reaction continued with the autocatalysis effect. The Cu pattern only forms in the scanned area, which demonstrates the catalytic activity of the laser-irradiated region. In Figure 1b,c, a metalized panda fabricated by this method is shown for demonstration. In addition, a quick response code was fabricated with high accuracy, as seen from Movie S1 (the code could be detected with a mobile app and enabled a link to a public website successfully). By FLAMD, metallization of the surface convex microarray could also be easily realized (Figure 1d) with a low sheet resistance (21 mΩ $sq.^{-1}$), which could be introduced in pressure sensors and triboelectric nanogenerators.[46,47] More details about the metallization of the convex surface microarray can be found in Supplementary Note 3.

Using nickel acetate ($NiAc_2$) instead of $CuAc_2$, Ni could be deposited on PDMS in a similar way (Figure 1e). As shown in Figure 1f,g, with predeposited Cu and Cu/Ni, Ag and Au could be further deposited on PDMS by replacement reaction and the autocatalysis effect. Note that a thin Ni layer is usually deposited between Cu and Au as a barrier layer to prevent the rapid diffusion of Cu to the Au surface. In addition, Cu could be deposited on other materials including PET, paper, Si, and glass (Supplementary Note 4 and Figure 5f). For PET, Si, and glass, to adhere to the catalyst precursor, the substrate surfaces were painted with a layer of $CuAc_2$ slurry. For paper, it was immersed in an aqueous solution containing $CuAc_2$. More details about the fabrication process can be found in the Experimental Section.

https://doi.org/10.1021/acsami.2c00419
ACS Appl. Mater. Interfaces 2022, 14, 11971−11980

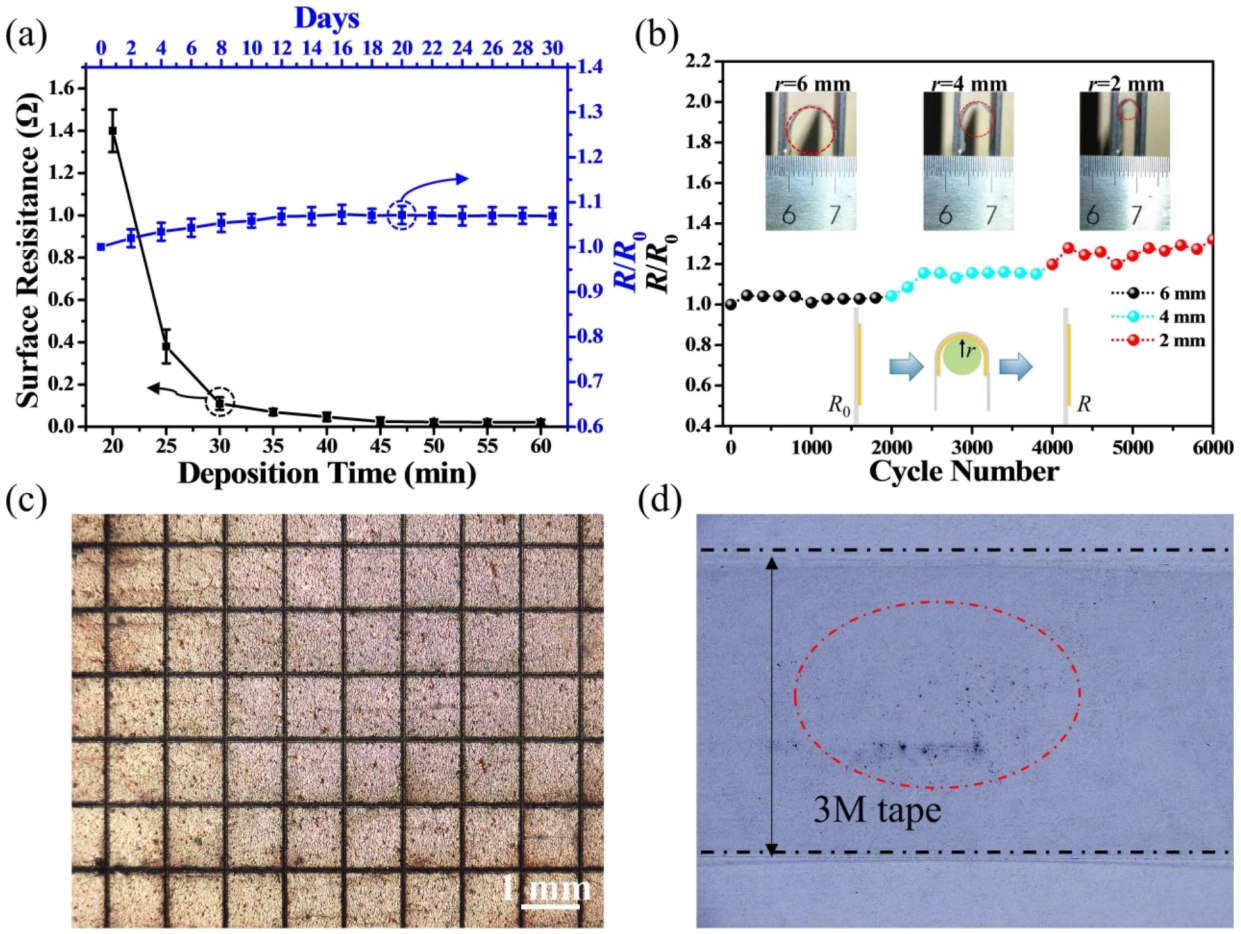

Figure 4. (a) Change of the electrical resistance of the Cu layer with the increase of the ELD time and the storage time under 25 °C/50% RH in the air, respectively. (b) Curve of the normalized electrical resistance (R/R_0) vs the number of the bending cycles for PDMS/Cu. The inset shows the schematic of the bending test. (c) Optical image of the sample after 20,000 bending cycles. The squares (1 mm × 1 mm each) were fabricated by laser cutting. (d) Optical image of the 3 M tape after the scotch tape test.

Therefore, FLAMD has fair generality in the preparation of metal electrodes. In this work, PDMS/Cu was used for property tests.

3. RESULTS AND DISCUSSION

3.1. Morphology and Composition Characterization. The morphologies of the substrates after femtosecond laser activation and ELD were characterized with a scanning electron microscope (SEM) and a transmission electron microscope (TEM). There are numerous coral-like microstructures with the size of several micrometers distributed on the sample surface after femtosecond laser activation (Figure 2a). The surface of the microscale corals is further decorated with abundant nanoscale protrusions (Figure 2b), forming a rough hierarchical structure. This structure may enhance the adhesion between the substrate and the Cu coating through the mechanical penetrating anchorage effect. The irradiated substrates were further investigated by the TEM (Figure 2c), which shows that the particle-like materials likely have melted together and generate irregular shapes. The high-resolution TEM image (Figure 2d) shows clear lattice fringes with *d*-spacings of 1.81 and 2.09 Å, corresponding to the (200) and the (111) lattice planes of Cu, respectively.[48] Another lattice fringe, measured as around 2.18 Å, matches well with the *d*-spacing of the (200) plane of β-SiC.[49] Besides, the SEM images (Figure 2e,f) reveal the continuous morphology of the Cu layer after ELD for 60 min, which is composed of aggregated Cu particles. Moreover, to determine the precision of the method, we prepared a narrow Cu wire. According to the diffraction limit, the laser wavelength (515 nm in this work) and the numerical aperture (NA) of the focusing objective lens both determine the precision. In this work, when the NA is 0.42 (M Plan Apo 20×, Mitutoyo, Japan) and the diameter of spot size before focusing is 2.54 mm, the width of the Cu wire is 3.14 μm measured by SEM and energy-dispersive X-ray (EDX) mapping (Figure 2g,h).

In addition, X-ray photoelectron spectroscopy (XPS) and X-ray diffraction (XRD) were adopted to unravel the chemical composition of the products. To facilitate the test, a substrate doped with 15 wt % $CuAc_2$ was used for characterization. As the high-resolution XPS Cu 2p spectra (Figure 3a) show, the Cu^{2+} peaks appear at 954.4 eV (Cu $2p_{1/2}$) and 934.4 eV (Cu $2p_{3/2}$) along with three concomitant satellites (940.4, 944.1, and 962.5 eV) before femtosecond laser activation, while two new peaks appear at 952.8 eV (Cu $2p_{1/2}$) and 932.7 eV (Cu $2p_{3/2}$) after femtosecond laser activation, which are ascribed to generation of Cu^0 (element copper).[50] The produced Cu^0 serves as a catalyst to trigger ELD. A shift of about 0.2 eV between the Cu 2p peaks before and after femtosecond laser activation reveals that the introduction of Cu^0 affects the electronic structure of Cu^{2+}, suggesting strong bonding between the product and the precursor[18] because of the in situ conversion approach. The XRD results shown in Figure 3b also confirm the above

https://doi.org/10.1021/acsami.2c00419
ACS Appl. Mater. Interfaces 2022, 14, 11971−11980

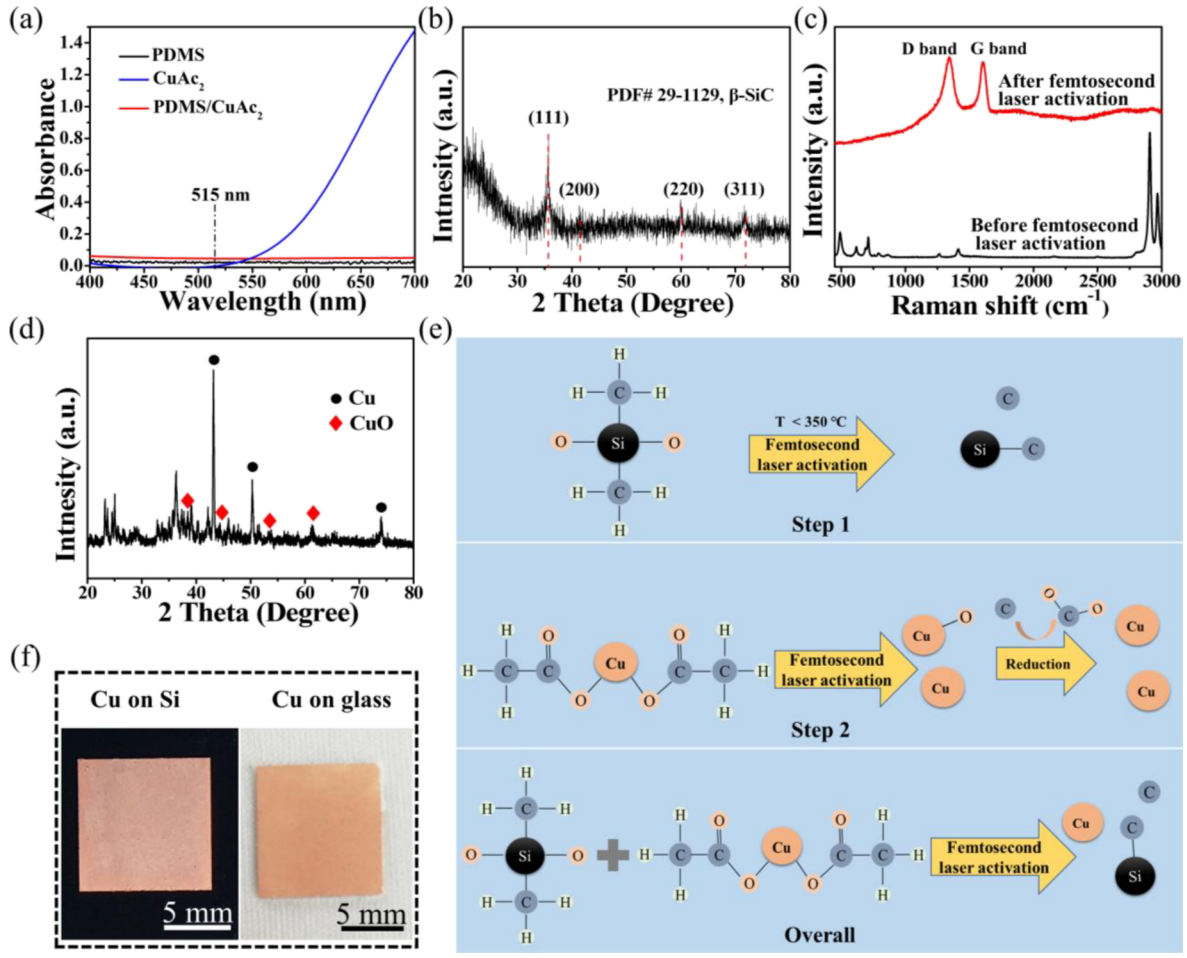

Figure 5. (a) UV−VIS spectra of native PDMS, $CuAc_2$ solution, and PDMS doped with 1 wt % $CuAc_2$. (b) XRD spectrum of the products of native PDMS after femtosecond laser activation. (c) Raman spectra of the sample before and after femtosecond laser activation. (d) XRD spectrum of the products of native $CuAc_2$ after femtosecond laser activation. (e) Schematic of the decomposition mechanism of PDMS/$CuAc_2$ under femtosecond laser activation. (f) Photographs of the obtained Cu coating on Si and glass by FLAMD.

explanation. Compared with the XRD spectrum of the substrate, there are three peaks featuring a Cu cubic structure (PDF# 04-0836) residing at 43.2°, 50.4°, and 74.1° after femtosecond laser activation, indicating that Cu^{2+} is reduced to Cu^0. Besides, no extra peaks are detected after ELD, showing that the obtained Cu layer possesses high purity.

3.2. Electrical and Mechanical Characterization. To assess the fabrication quality, we fabricated a 10 mm × 2 mm Cu region by FLAMD. As shown in Figure 4a, the electrical resistance measured with a digital multimeter decreases with a longer deposition time from the black curve. At the initial stage of ELD, the Cu layer may be discontinuous when the deposition time is less than 20 min and, therefore, cannot form a conductive path. With the extension of the deposition time, the continuity of the Cu layer improves, and the electrical resistance gradually decreases. After 60 min, the electrical resistance of Cu is 0.021 Ω. The electrical conductivity is determined using the following equation $\sigma = l/Rwd$, where σ is the electrical conductivity, l is the length, R is the electric resistance, w is the width, and d is the thickness. According to the cross-section image (Supplementary Note 5), the thickness of the Cu layer is 6.35 μm. Therefore, σ is calculated to be 3.75×10^7 S m^{-1}, which is slightly lower than that of high purity bulk Cu (5.96×10^7 S m^{-1}). Moreover, the stability of the coating can be evaluated by using the curve of the normalized electrical resistance (R/R_0) vs the extension of storage days under 25 °C and 50% relative humidity (RH) in the air, where R and R_0 are the electrical resistances of the Cu layer after and before the storage, respectively. From the blue curve in Figure 4a, the electrical resistance of the Cu layer slightly increases with the extension of storage time. After 18-day storage, the electrical resistance remains stable. These phenomena could be explained by the formation and stabilization of an oxidation layer on the surface of the Cu coating, which is confirmed by EDX and XPS characterization shown in Supplementary Note 6. A thin oxide layer can easily form on the Cu surface under ambient conditions,[51,52] resulting in an increase in the electrical resistance of the Cu coating.[53]

Flexible electrodes must be deformable with the electrical conductivity remaining stable, so the test of their reliability under mechanical bending is essential. The bending test results of the as-fabricated PDMS/Cu electrode are shown in Figure 4b. A Cu line with a length of 40 mm and a width of 2 mm was fabricated on a PDMS substrate and was bent at different radii of curvature (r) for 2000 cycles to record the change in the electrical resistance. These tests were performed continuously on the same sample. As shown in the inset of Figure 4b, the flexibility can be characterized using the curve of the normalized resistance (R/R_0) vs the number of the bending cycles, where R and R_0 are the electrical resistances of the Cu line after and before the bending test, respectively. The normalized resistance

https://doi.org/10.1021/acsami.2c00419
ACS Appl. Mater. Interfaces 2022, 14, 11971−11980

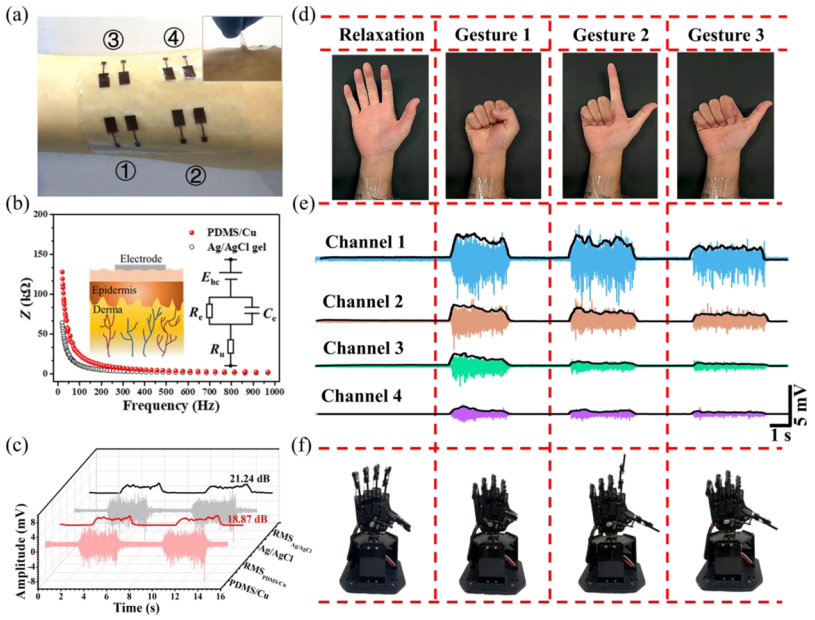

Figure 6. (a) Photograph of the customized PDMS/Cu electrode array laminated on the forearm of the subject. The inset shows the conformal contact at the electrode−skin interface. (b) Contact impedance between different electrodes and human skin. The insets illustrate an equivalent circuit model of the electrode−skin interface. E_{hc}: half-cell potential between skin and the electrode. C_e and R_e: capacitance and resistance of the epidermis layer. R_u: resistance of the underlying derma. (c) Characteristics of the recorded sEMG signals. The RMS plots of the sEMG signals were calculated from the raw data, and the SNR data were calculated from the RMS signals. (d) Images showing human hand gestures. (e) Characteristics of the sEMG signals from the channels during three hand gestures in (d). Black lines represent the RMS plots. (f) Corresponding gestures of a robot hand.

can remain stable at 1.0 during the initial stage, then gradually increases from 1.0, and finally reaches 1.3 when r is 2.0 mm. The results demonstrate that the electrical resistance at each step of deformation does not have obvious changes.

Besides, the scotch tape test, a common method for evaluating the adhesion strength, was used to examine the bonding between the deposited Cu coating and the PDMS substrate. The PDMS/Cu film was bent for 10,000 cycles at r = 3 mm and then was divided into 100 squares (1 mm × 1 mm each) by laser cutting. The cutting depths in both directions are greater than the thickness of Cu coating (6.35 μm). None of the cross-hatched squares was stripped after being quickly peeled off vertically the film, suggesting the best level (ASTM D3359 standard). More details are described in Supplementary Note 7. After the first tape test, the sample was bent for another 10,000 cycles at r = 3 mm, which still maintains the best level as illustrated in Figure 4c. As indicated by Figure 4d, only a trace of powders that might be produced by the dividing process remains on the 3 M tape and no Cu pieces are found.

3.3. Chemical Reactions under Femtosecond Laser Activation. Investigations were performed to infer the mechanism of Cu^0 generation resulting from the interaction between the femtosecond laser and the PDMS/$CuAc_2$ film. Native PDMS, $CuAc_2$ solution, and PDMS/$CuAc_2$ are almost transparent at 515 nm from the linear absorption spectra (Figure 5a), so nonlinear optical absorption is involved during femtosecond laser activation. According to previous studies, with conventional furnace heating, a siloxane preceramic polymer can convert to SiC when the temperature is above 1400 °C within an inert ambiance,[54] while $CuAc_2$ could be decomposed into Cu^0 and copper oxide (CuO) when the temperature is higher than its decomposition temperature.[55] β-SiC after femtosecond laser activation of native PDMS is detected from XRD (Figure 5b), while the D and G bands (1350 and 1590 cm^{-1}) of carbon are detected from the Raman spectrum (Figure 5c), although the temperature induced by femtosecond laser irradiation is about 350 °C, much lower than 1400 °C, from a thermal camera as shown in Supplementary Note 8. Note: The intensity of the XRD peaks for β-SiC might be too low to be found in the XRD result for the sample doped with 15 wt % $CuAc_2$ after femtosecond laser activation (Figure 3b). Moreover, the Raman bands from SiC are often too weak to be detected in the presence of carbon,[56] which can be attributed to the lower Raman scattering efficiency of SiC than that of carbon.[57] The phenomenon is consistent with other reports for processing siloxane polymers with a laser.[58,59] A kinetic effect of decomposition may be involved, by which rapid heating could cause decomposition of PDMS at a lower temperature.[60] Therefore, we speculate that the rapid temperature rise caused by femtosecond laser heating leads to the decomposition of PDMS. The rapid heating could directly initiate Si−O and C−H bond scission, generating β-SiC and carbon within a low-temperature range. In contrast, from thermogravimetry analysis of $CuAc_2$ (Supplementary Note 9), the decomposition temperature of $CuAc_2$ (250 °C) is lower than the temperature induced by femtosecond laser activation. It is proven from XRD (Figure 5d) that $CuAc_2$ could be decomposed into Cu^0 and CuO by femtosecond laser heating. The oxidation peaks are relatively strong after femtosecond laser activation of native $CuAc_2$, while there is no obvious oxidation peak for the irradiated products from PDMS/$CuAc_2$ (Figure 3b). The results show that the presence of PDMS provides a reducing environment probably because carbon generated from PDMS inhibits the formation of the oxide.

Combining the above, we propose a possible reaction mechanism for PDMS/$CuAc_2$ under femtosecond laser activation, as shown in Figure 5e. Under femtosecond laser activation, β-SiC and carbon come from the decomposition of PDMS, while Cu^0 originates from the direct decomposition of $CuAc_2$ and the reduction of CuO by carbon. Therefore, carbon

https://doi.org/10.1021/acsami.2c00419
ACS Appl. Mater. Interfaces 2022, 14, 11971−11980

plays a supplementary role in promoting the formation of Cu^0. Compared with the previous work using the nanosecond laser,[44] the method using the femtosecond laser shows two merits. First, it alleviates the restriction on absorbing sensitizers since the high instantaneous intensity of the femtosecond laser can induce nonlinear absorption, for example, in PDMS and $CuAc_2$ in this work. Moreover, it is unnecessary to use polymer substrates as carbon sources for generating a Cu^0 catalyst with the femtosecond laser. This could be attributed to the ultrashort heating time using the femtosecond laser, during which a much smaller amount of Cu^0 is oxidized in air. We have corroborated the flexibility in substrate selection by successfully fabricating Cu coating on Si and glass (Figure 5f).

3.4. Applications and Prospect. In recent years, hand gesture recognition based on surface electromyography (sEMG) signals has received tremendous attention, which is exploited for human−machine interface (HMI) applications.[61,62] To acquire sEMG signals, flexible electrodes play a critical role in the signal-processing HMI systems. Due to the irregular spatial distribution of the forearm muscle groups, the information collected by a single bipolar channel is rather limited. According to the anatomy of the human forearm, several forearm muscles separately control the motion of each finger.[63] For high-accuracy gesture identification, a multichannel electrode array that could collect sEMG signals from these muscles is necessary. Owing to the capability for customization and the reliable electrical and mechanical properties of the flexible electrodes made by FLAMD, a multichannel electrode array for HMI applications could be easily fabricated, as illustrated in Figure 6a. The flexible electrodes can be directly mounted to achieve conformal contact with human skin (the inset of Figure 6a). The electrode−skin impedance characterizes the electric behavior of the contact interface, which is commonly modeled as a combination of RC elements (the insets in Figure 6b).[64] The electrode−skin impedance was measured with an LCR meter from 20 to 1020 Hz (the main frequency band of sEMG signals[65]) to characterize the electrical performance of the electrodes, as shown in Figure 6b. Commercial Ag/AgCl gel electrodes are chosen as a reference. It is observed that the impedance for the PDMS/Cu electrodes is slightly higher than that for the gel electrodes. However, the gel electrodes might incur significant measurement errors due to drying of the gel after long-time usage.[66,67]

In Figure 6c, the quality of sEMG signals recorded by different electrodes is compared. The fist-clenching gesture was tested twice with an interval of 4 s, and the gestures resulted in almost the same patterns of sEMG signals reflected by the root mean square (RMS). The signal-to-noise ratio (SNR) calculated using the RMS of the Ag/AgCl gel electrodes is 21.24 dB, while that of PDMS/Cu is slightly lower (18.87 dB), which shows that the PDMS/Cu electrodes have comparable fidelity to the commercial Ag/AgCl gel electrodes. Figure 6d displays three different finger gestures, and each gesture results in a different sEMG signal and RMS (Figure 6e). The RMS, as the feature of gesture recognition, could realize the gesture synchronization of a virtual hand (Supplementary Note 10 and Movie S2). To control a real robot hand accurately and effectively, we used the random forest machine learning model as the classifier to analyze gesture features (including RMS, mean absolute value, wavelength, zero cross, and slope sign change) and control the robot hand to follow the gestures (Figure 6f and Movie S3), which demonstrates the practical applications of the flexible electrodes to complete HMI tasks. More details about the model are described in Supplementary Note 11.

4. CONCLUSIONS

This work reported a feasible method, FLAMD, for mask-free and low-cost fabrication of flexible metal electrodes. Without complicated surface pretreatments and operations, FLAMD can easily deposit metals (Cu, Ni, Ag, and Au) on PDMS and other materials, including PET, paper, Si, and glass. The obtained Cu layer exhibits electrical conductivity comparable to that of bulk Cu and excellent adhesion with PDMS. Compared with the nanosecond laser fabrication methods, FLAMD releases the restriction on absorbing sensitizers and suppresses oxidation of catalysts in the air without polymer substrates due to the nonlinear absorption and ultrashort heating time of femtosecond laser processing. Thereby, it could be adapted to depositing metals on inorganic substrates, such as flexible glass. In addition, FLAMD benefits processing of temperature-sensitive flexible substrates like PDMS, due to the small heat-affected zone of femtosecond laser processing. The flexible electrodes have been successfully adopted to acquire the sEMG signals with high fidelity, enabling real-time control of a robot hand.

5. EXPERIMENTAL SECTION

5.1. Materials. PDMS was supplied by Dow Corning Corporation. PET, Si, glass, and paper were purchased by Taobao Co., Ltd. (Zhejiang, China). Other chemicals were purchased from Aladdin Industrial Co., Ltd. (Shanghai, China). Deionized Mini-Q water (18 MΩ cm) was used for all experiments.

5.2. Preparation of Samples. For PDMS/$CuAc_2$ or PDMS/$NiAc_2$, PDMS and 1 wt % $CuAc_2$ or 1 wt % $NiAc_2$ were first mixed uniformly using a high-speed mixer. After degassing, the liquid mixture was dropped onto a glass sheet for spin-coating and cured at 80 °C for 30 min to obtain a piece of film with a thickness of ∼100 μm. PDMS for robot control was prepared with a mixture of precursor and crosslinker at a 20:1 ratio, and the other samples in this work were prepared at 10:1. For PET, Si, and glass, the substrate surfaces were painted with a layer of slurry (1 g of $CuAc_2$ and 5 mL of ethanol) and then were dried at 80 °C for 1 h. For paper, it was immersed in an aqueous solution (<5 wt % $CuAc_2$) for 5 min and then was dried at 80 °C for 1 h. The aqueous solution of $CuAc_2$ (5 wt % $CuAc_2$) was prepared for the UV−vis absorption test.

5.3. Femtosecond Laser Activation. The laser activation experiment was conducted with a homemade processing system. An Yb: KGW femtosecond laser (Pharos-10 W, Light Conversion) with a center wavelength of 515 nm (second-harmonic generation) was used as the laser source, which is widely used in industry for laser processing because of its high average power, low cost, long lifetime, insensitivity to environmental disturbance, and wider tuning range of repetition rates. The laser was focused on the sample surface using a lens with a 5 cm focal length. The laser system was equipped with a 3D translational platform. In this work, the fluence, the scanning speed, and the repetition rate were 22 mJ cm^{-2}, 10 mm s^{-1}, and 50 kHz, respectively, unless specified. The line-by-line scanning method for pattern generation was used in this work with an interval of 15 μm.

5.4. Metallization by ELD. ELD of Cu was performed in a plating bath consisting of a 1:1 mixture of solutions A and B at 40 °C for 1 h. Solution A was a DI water solution of copper sulfate pentahydrate (14 g L^{-1}), sodium hydroxide (14 g L^{-1}), potassium sodium tartrate (14 g L^{-1}), ethylenediaminetetraacetic acid (20 g L^{-1}), and potassium ferrocyanide (10 mg L^{-1}). Solution B was a formaldehyde aqueous solution (12 mL L^{-1}). For ELD of Ni, PDMS/$NiAc_2$ after femtosecond laser activation was immersed in a plating bath consisting of nickel sulfate pentahydrate (30 g L^{-1}), sodium citrate (10 g L^{-1}), ammonia chloride (30 g L^{-1}), and sodium hypophosphite (30 g L^{-1}) in DI water at 70 °C for 1.5 h, and the pH was adjusted to 10.0 with ammonia. For ELD of Ag, PDMS/$CuAc_2$ after femtosecond laser activation was immersed in the solution for ELD of Cu at 40 °C for 20 min followed by immersion in an Ag plating bath (silver ammonia solution: 0.5 g of silver

https://doi.org/10.1021/acsami.2c00419
ACS Appl. Mater. Interfaces 2022, 14, 11971−11980

nitrate was dispersed in 50 mL of DI water, and then, ammonia−water solution was dropped to achieve pH of 10−11. Reducing agent solution: 1 mL of formaldehyde) at room temperature for 1 h. For ELD of Au, a thin Ni layer was first deposited onto the Cu surface with the help of an iron nail followed by immersion in an Au plating bath (3.39 g L^{-1} chloroauric acid, 0.4 g L^{-1} sodium hydroxide, 11 g L^{-1} sodium hypophosphite, and 16 g L^{-1} sodium thiosulfate pentahydrate in DI water) at 65 ° C for 1 h. After the deposition, the samples were rinsed with DI water and dried by nitrogen flow.

5.5. Recording of sEMG Signals. The sEMG signals were recorded on a homemade EMG monitor based on an Arduino Uno Rev3 board with four channels. Each channel contained three electrodes, two of which were pasted on the forearm to detect the sEMG signals, and the other one (this one is a commercial Ag/AgCl gel electrode) was attached at the back of the elbow. Commercial electrodes (Xunda Ag/AgCl gel electrodes) and PDMS/Cu electrodes were used for comparison. On-skin experiments were conducted under approval from the Southern University of Science and Technology, Human Participants Ethics Committee (Protocol Number: 20210090).

5.6. Characterization. Morphologies and structures were observed by field emission scanning electron microscopy (FEI Nova Nano SEM 450) and high-resolution transmission electron microscopy (Tecnai G2F20 FEI), respectively. The crystalline structure was obtained by XRD (Rigaku D/Max2500, Japan) with a Cu Kα radiation source (λ = 1.5406 Å). An X-ray photoelectron spectrometer (PHI-1800, Japan) was used to measure the surface element composition and chemical state of the as-prepared samples. Raman spectra were measured using a Raman spectrometer (HORIBA LabRAM HR Evolution) with 532 nm laser excitation. The electrode−skin impedance was measured with an LCR meter (IM3533-01, HIOKI). The electrical resistance was measured with a digital multimeter (DMM 6500, Keithley). The absorption spectra were measured with a UV/VIS/NIR spectrometer (Lambda 750 S, PerkinElmer). Thermogravimetric (TG) analysis was performed using a TG analyzer (STA 2500 Regulus, NETZSCH) at a heating rate of 20 °C/min in air. The surface profile of the Cu coating was studied with a confocal laser scanning microscope (VK-X1000, Keyence). The temperature of the sample was measured with an infrared camera (T660, FLIR Systems Inc.). The sheet resistance was measured using a four-point probe system (RTS-8, Guangzhou 4-probe Tech Co. Ltd.) with a probe spacing of ∼1 mm.

■ ASSOCIATED CONTENT

Supporting Information

The Supporting Information is available free of charge at https://pubs.acs.org/doi/10.1021/acsami.2c00419.

UV−vis spectrum of the PDMS/$CuAc_2$ film (Figure S1); optical images of the obtained Cu coatings (Figure S2); laser activation with and without a dust cleaner (Figure S3); the obtained Cu coating at different deposition times (Figure S4); the obtained Cu on PET and paper (Figure S5); cross-sectional SEM image of Cu coating (Figure S6); typical EDX spectra of the Cu coating (Figure S7); XPS spectra of the Cu coating with different exposure times (Figure S8); Cu LMM spectra of the Cu coating with different exposure times (Figure S9); the results of the scotch tape test (Figure S10); experimental setup for temperature monitoring (Figure S11); effect of the temperature rise rate on decomposition of PDMS (Figure S12); TG curve of $CuAc_2$ (Figure S13); the corresponding gestures of a virtual hand (Figure S14); the flow chart of gesture recognition (Figure S15); and the hardware system of gesture recognition (Figure S16) (PDF)

Quick response code detected with a mobile app (Movie S1) (MP4)

The gesture synchronization of a virtual hand (Movie S2) (MP4)

Robot hand (Movie S3) (MP4)

■ AUTHOR INFORMATION

Corresponding Authors

Hongqiang Wang − *Department of Mechanical and Energy Engineering, Shenzhen Key Laboratory of Biomimetic Robotics and Intelligent Systems, Department of Mechanical and Energy Engineering, and Guangdong Provincial Key Laboratory of Human-Augmentation and Rehabilitation Robotics in Universities, Southern University of Science and Technology, Shenzhen 518055, China*; Email: wanghq6@sustech.edu.cn

Liang Guo − *Department of Mechanical and Energy Engineering, Southern University of Science and Technology, Shenzhen 518055, China*; orcid.org/0000-0002-8134-5574; Email: guol3@sustech.edu.cn

Authors

Yaqiang Ji − *School of Mechanical Engineering, Harbin Institute of Technology, Harbin 150080, China; Department of Mechanical and Energy Engineering, Southern University of Science and Technology, Shenzhen 518055, China*

Yuxuan Liao − *Department of Mechanical and Energy Engineering and Shenzhen Key Laboratory of Biomimetic Robotics and Intelligent Systems, Department of Mechanical and Energy Engineering, Southern University of Science and Technology, Shenzhen 518055, China*

Haihui Li − *Department of Mechanical and Energy Engineering, Southern University of Science and Technology, Shenzhen 518055, China*

Yuhang Cai − *Department of Mechanical and Energy Engineering, Southern University of Science and Technology, Shenzhen 518055, China*

Dongliang Fan − *Department of Mechanical and Energy Engineering and Shenzhen Key Laboratory of Biomimetic Robotics and Intelligent Systems, Department of Mechanical and Energy Engineering, Southern University of Science and Technology, Shenzhen 518055, China*

Qian Liu − *Department of Mechanical and Energy Engineering, Southern University of Science and Technology, Shenzhen 518055, China*

Shubin Huang − *Department of Mechanical and Energy Engineering, Southern University of Science and Technology, Shenzhen 518055, China*

Renjie Zhu − *Department of Mechanical and Energy Engineering and Shenzhen Key Laboratory of Biomimetic Robotics and Intelligent Systems, Department of Mechanical and Energy Engineering, Southern University of Science and Technology, Shenzhen 518055, China*

Shuai Wang − *Department of Mechanical and Energy Engineering, Southern University of Science and Technology, Shenzhen 518055, China*

Complete contact information is available at: https://pubs.acs.org/10.1021/acsami.2c00419

Author Contributions

Y.J. conducted most of the experiments and wrote the manuscript. Y.L. performed the test of the virtual hand. H.L. helped with the control of the robotic hand. Y.C. and D.F. contributed key ideas. Q.L. conducted TEM characterizations. S.H., R.Z., and S.W. contributed to the analysis and discussion. H.W. and L.G. supervised the whole process.

https://doi.org/10.1021/acsami.2c00419
ACS Appl. Mater. Interfaces 2022, 14, 11971−11980

Notes

The authors declare no competing financial interest.

■ ACKNOWLEDGMENTS

The FLAMD development was supported by the National Key Research and Development Program of China (2020YFA0715000), the Natural Science Foundation of Guangdong Province (2019A1515010745), and Shenzhen Science and Technology Program (KQTD20170810110250357). The HMI application was supported by the National Natural Science Foundation for Young Scientists of China (51905256), the Natural Science Foundation of Guangdong Province of China (2020A1515010955), and the Science, Technology and Innovation Commission of Shenzhen Municipality (ZDSYS20200811143601004).

■ REFERENCES

(1) Kim, Y.; Chortos, A.; Xu, W.; Liu, Y.; Oh, J. Y.; Son, D.; Kang, J.; Foudeh, A. M.; Zhu, C.; Lee, Y. A bioinspired flexible organic artificial afferent nerve. *Science* **2018**, *360*, 998−1003.

(2) Li, W.; Torres, D.; Díaz, R.; Wang, Z.; Wu, C.; Wang, C.; Wang, Z. L.; Sepúlveda, N. Nanogenerator-based dual-functional and self-powered thin patch loudspeaker or microphone for flexible electronics. *Nat. Commun.* **2017**, *8*, 1−9.

(3) Liang, J.; Li, L.; Niu, X.; Yu, Z.; Pei, Q. Elastomeric polymer light-emitting devices and displays. *Nat. Photon.* **2013**, *7*, 817−824.

(4) White, M. S.; Kaltenbrunner, M.; Głowacki, E. D.; Gutnichenko, K.; Kettlgruber, G.; Graz, I.; Aazou, S.; Ulbricht, C.; Egbe, D. A.; Miron, M. C. Ultrathin, highly flexible and stretchable PLEDs. *Nat. Photon.* **2013**, *7*, 811−816.

(5) Zhou, M.; Wu, Z.; Zhao, Y.; Yang, Q.; Ling, W.; Li, Y.; Xu, H.; Wang, C.; Huang, X. Droplets as carriers for flexible electronic devices. *Adv. Sci.* **2019**, *6*, No. 1901862.

(6) Park, H. L.; Lee, Y.; Kim, N.; Seo, D. G.; Go, G. T.; Lee, T. W. Flexible neuromorphic electronics for computing, soft robotics, and neuroprosthetics. *Adv. Mater.* **2020**, *32*, No. 1903558.

(7) Yeo, W. H.; Kim, Y. S.; Lee, J.; Ameen, A.; Shi, L.; Li, M.; Wang, S.; Ma, R.; Jin, S. H.; Kang, Z. Multi-functional electronics: multifunctional epidermal electronics printed directly onto the skin. *Adv. Mater.* **2013**, *25*, 2772−2772.

(8) Cao, Y.; Tan, Y. J.; Li, S.; Lee, W. W.; Guo, H.; Cai, Y.; Wang, C.; Tee, B. C.-K. Self-healing electronic skins for aquatic environments. *Nat. Electron.* **2019**, *2*, 75−82.

(9) Tao, X.; Liao, S.; Wang, Y. Polymer-assisted fully recyclable flexible sensors. *EcoMat* **2021**, *3*, e12083.

(10) Ma, B.; Xu, C.; Chi, J.; Chen, J.; Zhao, C.; Liu, H. A versatile approach for direct patterning of liquid metal using magnetic field. *Adv. Funct. Mater.* **2019**, *29*, No. 1901370.

(11) Wang, J.; Cai, G.; Li, S.; Gao, D.; Xiong, J.; Lee, P. S. Printable superelastic conductors with extreme stretchability and robust cycling endurance enabled by liquid-metal particles. *Adv. Mater.* **2018**, *30*, No. 1706157.

(12) Hamzah, H. H.; Shafiee, S. A.; Abdalla, A.; Patel, B. A. 3D printable conductive materials for the fabrication of electrochemical sensors: a mini review. *Electrochem. Commun.* **2018**, *96*, 27−31.

(13) Yu, L.; Shearer, C.; Shapter, J. Recent development of carbon nanotube transparent conductive films. *Chem. Rev.* **2016**, *116*, 13413−13453.

(14) Zhang, Q.; Liu, L.; Pan, C.; Li, D. Review of recent achievements in self-healing conductive materials and their applications. *J. Mater. Sci.* **2018**, *53*, 27−46.

(15) Chen, J.; Yu, Q.; Cui, X.; Dong, M.; Zhang, J.; Wang, C.; Fan, J.; Zhu, Y.; Guo, Z. An overview of stretchable strain sensors from conductive polymer nanocomposites. *J. Mater. Chem. C* **2019**, *7*, 11710−11730.

(16) Li, P.; Zhang, Y.; Zheng, Z. Polymer-assisted metal deposition (PAMD) for flexible and wearable electronics: principle, materials, printing, and devices. *Adv. Mater.* **2019**, *31*, No. 1902987.

(17) Lu, X.; Zhang, Y.; Zheng, Z. Metal-based flexible transparent electrodes: challenges and recent advances. *Adv. Electron. Mater.* **2021**, *7*, No. 2001121.

(18) Sun, G.; Jin, X.; Yang, H.; Gao, J.; Qu, L. An aqueous Zn-MnO_2 rechargeable microbattery. *J. Mater. Chem. A* **2018**, *6*, 10926−10931.

(19) Shi, J.; Wang, S.; Chen, X.; Chen, Z.; Du, X.; Ni, T.; Wang, Q.; Ruan, L.; Zeng, W.; Huang, Z. An ultrahigh energy density quasi-solid-state zinc ion microbattery with excellent flexibility and thermostability. *Adv. Energy Mater.* **2019**, *9*, No. 1901957.

(20) Radha, B.; Kulkarni, G. Dewetting assisted patterning of polystyrene by soft lithography to create nanotrenches for nanomaterial deposition. *ACS Appl. Mater. Interfaces* **2009**, *1*, 257−260.

(21) Xie, J.-Q.; Ji, Y.-Q.; Kang, J.-H.; Sheng, J.-L.; Mao, D.-S.; Fu, X.-Z.; Sun, R.; Wong, C.-P. In situ growth of $Cu(OH)_2$@FeOOH nanotube arrays on catalytically deposited Cu current collector patterns for high-performance flexible in-plane micro-sized energy storage devices. *Energy Environ. Sci.* **2019**, *12*, 194−205.

(22) Yan, J.; Lu, Y.; Chen, G.; Yang, M.; Gu, Z. Advances in liquid metals for biomedical applications. *Chem. Soc. Rev.* **2018**, *47*, 2518−2533.

(23) Kazem, N.; Hellebrekers, T.; Majidi, C. Soft multifunctional composites and emulsions with liquid metals. *Adv. Mater.* **2017**, *29*, No. 1605985.

(24) Rahim, M. A.; Centurion, F.; Han, J.; Abbasi, R.; Mayyas, M.; Sun, J.; Christoe, M. J.; Esrafilzadeh, D.; Allioux, F. M.; Ghasemian, M. B. Polyphenol-induced adhesive liquid metal inks for substrate-independent direct pen writing. *Adv. Funct. Mater.* **2021**, *31*, No. 2007336.

(25) Barhoum, A.; Samyn, P.; Öhlund, T.; Dufresne, A. Review of recent research on flexible multifunctional nanopapers. *Nanoscale* **2017**, *9*, 15181−15205.

(26) Guo, J. Z.; Gu, Z. Y.; Zhao, X. X.; Wang, M. Y.; Yang, X.; Yang, Y.; Li, W. H.; Wu, X. L. Flexible Na/K-ion full batteries from the renewable cotton cloth-derived stable, low-cost, and binder-free anode and cathode. *Adv. Energy Mater.* **2019**, *9*, No. 1902056.

(27) Kang, Z.; Zhang, Y.; Zhou, M. AgNPs@CNTs/Ag hybrid films on thiolated PET substrate for flexible electronics. *Chem. Eng. J.* **2019**, *368*, 223−234.

(28) Shen, L.; Wu, L.; Sheng, Q.; Ma, C.; Zhang, Y.; Lu, L.; Ma, J.; Ma, J.; Bian, J.; Yang, Y. Epitaxial lift-off of centimeter-scaled spinel ferrite oxide thin films for flexible electronics. *Adv. Mater.* **2017**, *29*, No. 1702411.

(29) Ippili, S.; Jella, V.; Eom, J.-H.; Kim, J.; Hong, S.; Choi, J.-S.; Tran, V.-D.; Van Hieu, N.; Kim, Y.-J.; Kim, H.-J. An eco-friendly flexible piezoelectric energy harvester that delivers high output performance is based on lead-free $MASnI_3$ films and $MASnI_3$-PVDF composite films. *Nano Energy* **2019**, *57*, 911−923.

(30) Deutz, D. B.; Mascarenhas, N. T.; Schelen, J. B. J.; de Leeuw, D. M.; Van der Zwaag, S.; Groen, P. Flexible piezoelectric touch sensor by alignment of lead-free alkaline niobate microcubes in PDMS. *Adv. Funct. Mater.* **2017**, *27*, No. 1700728.

(31) Gao, Z.; Lin, G.; Chen, Y.; Zheng, Y.; Sang, N.; Li, Y.; Chen, L.; Li, M. Moth-eye nanostructure PDMS films for reducing reflection and retaining flexibility in ultra-thin c-Si solar cells. *Sol. Energy* **2020**, *205*, 275−281.

(32) Kant, M. B.; Shinde, S. D.; Bodas, D.; Patil, K.; Sathe, V.; Adhi, K.; Gosavi, S. Surface studies on benzophenone doped PDMS microstructures fabricated using KrF excimer laser direct write lithography. *Appl. Surf. Sci.* **2014**, *314*, 292−300.

(33) Ye, X.; Cai, D.; Ruan, X.; Cai, A. Research on the selective adhesion characteristics of polydimethylsiloxane layer. *AIP Adv.* **2018**, *8*, 095004.

(34) Azzaroni, O.; Zheng, Z.; Yang, Z.; Huck, W. T. Polyelectrolyte brushes as efficient ultrathin platforms for site-selective copper electroless deposition. *Langmuir* **2006**, *22*, 6730−6733.

https://doi.org/10.1021/acsami.2c00419
ACS Appl. Mater. Interfaces 2022, 14, 11971−11980

(35) Liu, X.; Zhou, X.; Li, Y.; Zheng, Z. Surface-grafted polymer-assisted electroless deposition of metals for flexible and stretchable electronics. *Chem. − Asian J.* **2012**, *7*, 862−870.
(36) Yu, Y.; Yan, C.; Zheng, Z. Polymer-assisted metal deposition (PAMD): a full-solution strategy for flexible, stretchable, compressible, and wearable metal conductors. *Adv. Mater.* **2014**, *26*, 5508−5516.
(37) Garcia, A.; Polesel-Maris, J.; Viel, P.; Palacin, S.; Berthelot, T. Localized ligand induced electroless plating (LIEP) process for the fabrication of copper patterns onto flexible polymer substrates. *Adv. Funct. Mater.* **2011**, *21*, 2096−2102.
(38) Guo, R.; Yu, Y.; Xie, Z.; Liu, X.; Zhou, X.; Gao, Y.; Liu, Z.; Zhou, F.; Yang, Y.; Zheng, Z. Matrix-assisted catalytic printing for the fabrication of multiscale, flexible, foldable, and stretchable metal conductors. *Adv. Mater.* **2013**, *25*, 3343−3350.
(39) Li, B.; Yu, B.; Ye, Q.; Zhou, F. Tapping the potential of polymer brushes through synthesis. *Acc. Chem. Res.* **2015**, *48*, 229−237.
(40) Cai, J.; Lv, C.; Hu, C.; Luo, J.; Liu, S.; Song, J.; Shi, Y.; Chen, C.; Zhang, Z.; Ogawa, S. Laser direct writing of heteroatom-doped porous carbon for high-performance micro-supercapacitors. *Energy Storage Mater.* **2020**, *25*, 404−415.
(41) Wu, J.; Yin, K.; Li, M.; Wu, Z.; Xiao, S.; Wang, H.; Duan, J.-A.; He, J. Under-oil self-driven and directional transport of water on a femtosecond laser-processed superhydrophilic geometry-gradient structure. *Nanoscale* **2020**, *12*, 4077−4084.
(42) Yong, J.; Chen, F.; Yang, Q.; Du, G.; Shan, C.; Bian, H.; Farooq, U.; Hou, X. Bioinspired transparent underwater superoleophobic and anti-oil surfaces. *J. Mater. Chem. A* **2015**, *3*, 9379−9384.
(43) Zhang, H.; Zhang, J.; Su, G.; Zhou, T.; Zhang, A. Ultraviolet photodetector on flexible polymer substrate based on nano zinc oxide and laser-induced selective metallization. *Compos. Sci. Technol.* **2020**, *12*, No. 108045.
(44) Zhang, J.; Feng, J.; Jia, L.; Zhang, H.; Zhang, G.; Sun, S.; Zhou, T. Laser-induced selective metallization on polymer substrates using organocopper for portable electronics. *ACS Appl. Mater. Interfaces* **2019**, *11*, 13714−13723.
(45) Xu, H.; Zhang, J.; Feng, J.; Zhou, T. Fabrication of copper patterns on polydimethylsiloxane through laser-induced selective metallization. *Ind. Eng. Chem. Res.* **2021**, *60*, 8821.
(46) Xiong, Y.; Shen, Y.; Tian, L.; Hu, Y.; Zhu, P.; Sun, R.; Wong, C.-P. A flexible, ultra-highly sensitive and stable capacitive pressure sensor with convex microarrays for motion and health monitoring. *Nano Energy* **2020**, *70*, No. 104436.
(47) Li, Z.; Feng, H.; Zheng, Q.; Li, H.; Zhao, C.; Ouyang, H.; Noreen, S.; Yu, M.; Su, F.; Liu, R. Photothermally tunable biodegradation of implantable triboelectric nanogenerators for tissue repairing. *Nano Energy* **2018**, *54*, 390−399.
(48) Jin, M.; He, G.; Zhang, H.; Zeng, J.; Xie, Z.; Xia, Y. Shape-controlled synthesis of copper nanocrystals in an aqueous solution with glucose as a reducing agent and hexadecylamine as a capping agent. *Angew. Chem., Int. Ed.* **2011**, *50*, 10560−10564.
(49) Chen, J.-P.; Jia, H.; Liu, Z.; Kong, Q.-Q.; Hou, Z.-H.; Xie, L.-J.; Sun, G.-H.; Zhang, S.-C.; Chen, C.-M. Construction of C-Si heterojunction interface in SiC whisker/reduced graphene oxide aerogels for improving microwave absorption. *Carbon* **2020**, *164*, 59−68.
(50) Li, G.; Tu, J.; Wang, M.; Jiao, S. Cu_3P as a novel cathode material for rechargeable aluminum-ion batteries. *J. Mater. Chem. A* **2019**, *7*, 8368−8375.
(51) Zuo, Z.-J.; Li, J.; Han, P.-D.; Huang, W. XPS and DFT studies on the autoxidation process of Cu sheet at room temperature. *J. Phys. Chem. C* **2014**, *118*, 20332−20345.
(52) Iijima, J.; Lim, J.-W.; Hong, S.-H.; Suzuki, S.; Mimura, K.; Isshiki, M. Native oxidation of ultra high purity Cu bulk and thin films. *Appl. Surf. Sci.* **2006**, *253*, 2825−2829.
(53) Platzman, I.; Brener, R.; Haick, H.; Tannenbaum, R. Oxidation of polycrystalline copper thin films at ambient conditions. *J. Phys. Chem. C* **2008**, *112*, 1101−1108.
(54) Burns, G. T.; Taylor, R. B.; Xu, Y.; Zangvil, A.; Zank, G. A. High-temperature chemistry of the conversion of siloxanes to silicon carbide. *Chem. Mater.* **1992**, *4*, 1313−1323.
(55) Lin, Z.; Han, D.; Li, S. Study on thermal decomposition of copper (II) acetate monohydrate in air. *J. Therm. Anal. Calorim.* **2012**, *107*, 471−475.
(56) Ward, Y.; Young, R. J.; Shatwell, R. A. A microstructural study of silicon carbide fibres through the use of Raman microscopy. *J. Mater. Sci.* **2001**, *36*, 55−66.
(57) Sasaki, Y.; Nishina, Y.; Sato, M.; Okamura, K. Raman study of SiC fibres made from polycarbosilane. *J. Mater. Sci.* **1987**, *22*, 443−448.
(58) Stankova, N. E.; Atanasov, P. A.; Nedyalkov, N. N.; Stoyanchov, T.; Kolev, K.; Valova, E.; Georgieva, J.; St, A. A.; Amoruso, S.; Wang, X. Fs- and ns-laser processing of polydimethylsiloxane (PDMS) elastomer: comparative study. *Appl. Surf. Sci.* **2015**, *336*, 321−328.
(59) Gao, Y.; Li, Q.; Wu, R.; Sha, J.; Lu, Y.; Xuan, F. Laser direct writing of ultrahigh sensitive SiC-based strain sensor arrays on elastomer toward electronic skins. *Adv. Funct. Mater.* **2019**, *29*, No. 1806786.
(60) Camino, G.; Lomakin, S.; Lazzari, M. Polydimethylsiloxane thermal degradation Part 1. Kinetic aspects. *Polymer* **2001**, *42*, 2395−2402.
(61) Kwon, Y. T.; Kim, Y. S.; Kwon, S.; Mahmood, M.; Yeo, W. H. All-printed nanomembrane wireless bioelectronics using a biocompatible solderable graphene for multimodal human-machine interfaces. *Nat. Commun.* **2020**, *11*, 1−11.
(62) Wu, H.; Yang, G.; Zhu, K.; Liu, S.; Guo, W.; Jiang, Z.; Li, Z. Materials, devices, and systems of on-skin electrodes for electrophysiological monitoring and human-machine interfaces. *Adv. Sci.* **2021**, *8*, No. 2001938.
(63) Schwarz, R. J.; Taylor, C. The anatomy and mechanics of the human hand. *Artif. Limbs* **1955**, *2*, 22−35.
(64) He, K.; Liu, Z.; Wan, C.; Jiang, Y.; Wang, T.; Wang, M.; Zhang, F.; Liu, Y.; Pan, L.; Xiao, M. An on-skin electrode with anti-epidermal-surface-lipid function based on a zwitterionic polymer brush. *Adv. Mater.* **2020**, *32*, No. 2001130.
(65) Li, Z.; Guo, W.; Huang, Y.; Zhu, K.; Yi, H.; Wu, H. On-skin graphene electrodes for large area electrophysiological monitoring and human-machine interfaces. *Carbon* **2020**, *164*, 164−170.
(66) Ochia, R. S.; Cavanagh, P. R. Reliability of surface EMG measurements over 12 hours. *J. Electromyogr. Kines.* **2007**, *17*, 365−371.
(67) Posada-Quintero, H. F.; Rood, R. T.; Burnham, K.; Pennace, J.; Chon, K. H. Assessment of carbon/salt/adhesive electrodes for surface electromyography measurements. *IEEE J. Transl. Eng. Heal. Med.* **2016**, *4*, 1−9.

https://doi.org/10.1021/acsami.2c00419
ACS Appl. Mater. Interfaces 2022, 14, 11971−11980